A study on the crack presence effect on dynamical behavior of higher-order Quasi-3D composite steel-polymer concrete box section beams via DQFEM

Nassim Laouche
Department of Planning and Hydraulic Engineering, Higher National School of Hydraulics, Blida, Algeria
n.laouche@ensh.dz, https://orcid.org/0000-0002-1376-5032

Ahmed Saimi
Mechanical engineering Department, Faculty of Science and Technology, University Belhadj Bouchaib, Ain Temouchent, Algeria
ahmed.saimi@univ-temouchent.edu.dz, https://orcid.org/0000-0002-3722-2526

Ismail Bensaid
IS2M Laboratory, Mechanical engineering Department, Faculty of Technology, University Abou Beckr Beklaid, Tlemcen, Algeria
ismail.bensaid@univ-tlemcen.dz, https://orcid.org/0000-0003-4316-0648

Mouloud Dahmane
Department of Planning and Hydraulic Engineering, Higher National School of Hydraulics, Blida, Algeria
m.dahmane@ensh.dz, *https://orcid.org/0009-0001-2032-2141*

Hassen Ait Atmane
Department of Civil Engineering, Faculty of Civil Engineering and Architecture, University Hassiba Benbouali, Chlef, Algeria
aitatmane2000@yahoo.fr, https://orcid.org/0000-0001-7248-2975

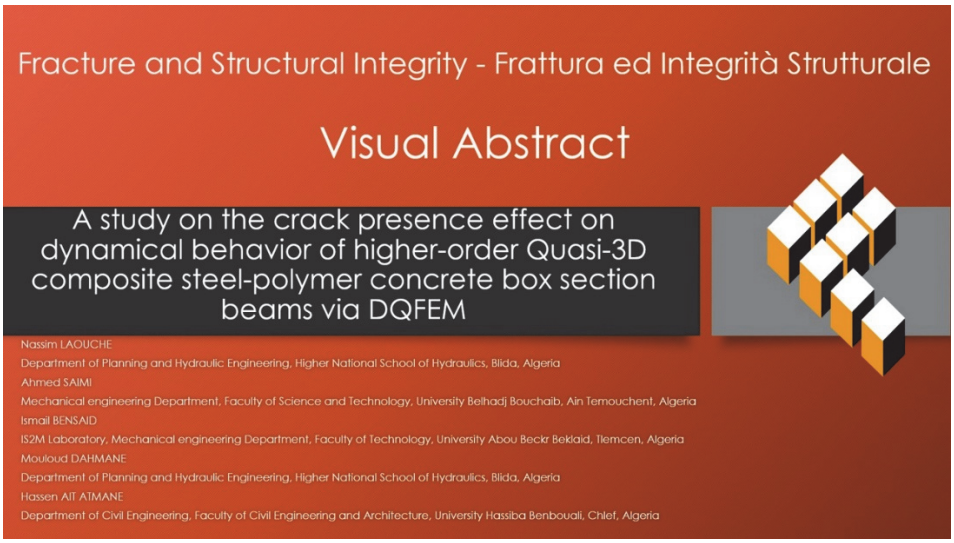

KEYWORDS. Quasi 3D beam theory, DQFEM, free vibration, critical buckling, composite beam, crack.

Citation: Laouche, N., Saimi, A., Bensaid, I., Dahmane, M., Ait Atmane, H., A study on the crack presence effect on dynamical behavior of higher-order Quasi-3D composite steel-polymer concrete box section beams via DQFEM, Fracture and Structural Integrity, 73 (2025) 88-107.

Received: 28.03.2025
Accepted: 09.05.2025
Published: 11.05.2025
Issue: 07.2025

INTRODUCTION

The study of composite beams has become increasingly significant due to their extensive applications in modern engineering structures, including bridges, aerospace systems, and machine tools [1]. Composite beams, particularly those integrating steel and polymer concrete, are pivotal in modern engineering applications due to their superior mechanical properties, such as high strength-to-weight ratios and enhanced durability [2]. Steel-polymer concrete composite systems leverage the ductility of steel and the compressive strength of polymer concrete, making them ideal for infrastructure, bridges, and high-performance structures [3]. However, the presence of cracks arising from material defects, fatigue, or external loads can significantly compromise their dynamic and stability characteristics, necessitating a thorough understanding of crack-induced effects on structural behavior [4].

The dynamic and buckling responses of composite beams have been extensively studied using various beam theories. Traditional models, such as the Timoshenko beam theory, have been employed to analyze the vibration behavior of steel-concrete composites, capturing shear deformation and rotational inertia effects. like the work of [5] who presented a solution of the problem of free vibrations of steel–concrete composite beams using three analytical models describing the dynamic behavior based on Euler beam theory, and on Timoshenko beam theory. [6] studied the dynamic behavior of Steel–Concrete Composite Beams Using the Euler-Bernoulli Beam Model via classical finite elements method and did also the experimental study. However, these models often simplify through-thickness deformations, limiting their accuracy for thick or heterogeneous sections. Advanced theories, including quasi-3D formulations, address this limitation by incorporating higher-order displacement fields, thereby improving the representation of complex stress distributions in multi-layered composites [7]. Concurrently, the Differential Quadrature Finite Element Method (DQFEM) has emerged as a powerful tool for solving structural mechanics problems, offering high computational efficiency and accuracy, particularly for beams with variable geometries or material properties. [8] studied the dynamic behavior of rotating shaft based on Euler Bernoulli beam theory via DQFEM. [9] proposed the DQFEM for the free vibration analysis of thin plates.

Recent advances in composite structures have highlighted their potential for improved mechanical and dynamic performance. Studies on porous sandwich plates show that foam cores can enhance vibration damping and natural frequencies [10]. At smaller scales, modified couple stress theory reveals size-dependent effects in functionally graded microplates and piezoelectric nano shells [11, 12]. Isogeometric and meshfree methods enable accurate modeling of complex geometries in active laminated shells [13, 14], while nonlinear buckling analyses demonstrate the influence of thermal-electromechanical loads on stability [15]. Additionally, surface treatments of carbon fibers have been shown to simultaneously improve damping and strength in CFRPs [16]. Building on these findings, this work investigates the interplay of material design, microstructural effects, and numerical modeling to optimize multifunctional composites.

Despite these advancements, existing studies on cracked composite beams remain limited. Most analyses focus on homogeneous or functionally graded materials. [17] investigated the Effect of crack presence on the dynamic and buckling responses of bidirectional functionally graded beams based on quasi-3D beam model and differential quadrature finite element method. Also another same study on bidirectional functionally graded microbeams with presence of crack by [18] was conducted. [19] investigated the Modal analysis of cracked functionally graded material beam with piezoelectric layer. [20] conducted a modal analysis of cracked functionally graded Timoshenko beam. [21] studied the crack's effect on the natural frequencies of bi-directional functionally graded beam. [22] studied an analytical model of longitudinal fracture in two-dimensional functionally graded beam with clamped free boundary conditions configurations with taking into account the non-linear behavior of material. [23] contributed to the analysis of the behavior of pre-cracked reinforced concrete composite beams with carbon fiber fabric and epoxy resin. [4] investigated the dynamic response of Euler–Bernoulli imperfect functionally graded (FG) cracked beams on Winkler-elastic foundation, considering pinned–pinned boundary condition. [24] investigated a numerical simulation on the effect of flexural crack on plain concrete beam failure mechanism. Furthermore, the simultaneous consideration of dynamic and buckling behaviors under crack-induced perturbations is underexplored, particularly for steel-polymer concrete systems. This gap underscores the need for a refined approach that integrates crack effects into a comprehensive mechanical framework.

In this study, a refined quasi-3D beam theory is employed to investigate the dynamic and critical buckling behavior of steel-polymer concrete composite beams with cracks in both the inner concrete core and outer steel box. The governing equations are derived using DQFEM combined with Lagrange's principle, accounting for slenderness ratios and beam thicknesses. The model's accuracy is validated against numerical and experimental results from literature, ensuring robustness. By systematically analyzing natural frequencies and critical buckling loads under varying crack depths and locations, this research provides critical insights into the performance of cracked composite beams. The findings aim to inform design guidelines for optimizing material-based structures, enhancing safety and reliability in engineering applications.

FORMULATION AND THEORIES

Steel-Polymer Concrete Beam Model

The concept of the steel-polymer concrete beam combines the synergistic properties of steel and polymer concrete to achieve enhanced mechanical performance, including stiffness, vibration energy dissipation, and dynamic adaptability. The beam structure includes a steel profile of length L with a square cross-section of thickness × width (h × b) and e_s wall thickness, filled with polymer concrete (Fig. 1). The bonding between the steel layer and the inner polymer concrete core is assumed to be perfect, implying no relative slip or separation at the interface under applied loads. The polymer concrete core is composed of epoxy resin and mineral fillers of varying grain sizes, including ash, fine sand, medium gravel, and coarse gravel, ensuring optimized density and strength distribution [6]. By controlling the arrangement and degree of filling, the dynamic properties of such composite beams can be tailored to meet specific structural requirements.

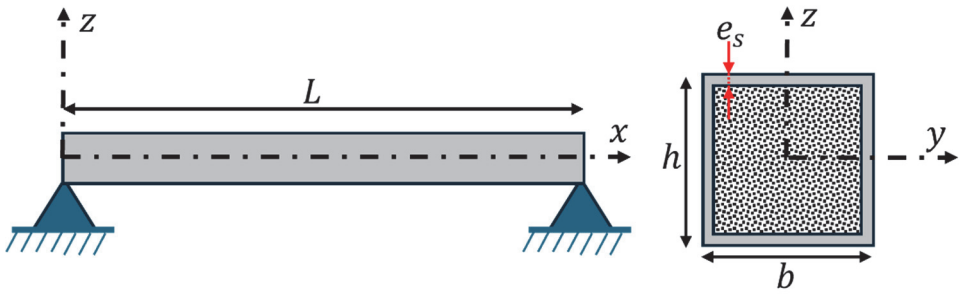

Figure 1: Box-Section Beam with Composite Infill.

Quasi-3D Beam Model

This study employs a higher-order quasi-3D beam formulation, where the displacement distribution at any point along the beam is represented as follows:

$$\begin{cases} u_1(x,z,t) = u(x,t) - z\dfrac{dw_b(x,t)}{dx} + f_1(z)\dfrac{dw_s(x,t)}{dx} \\ u_3(x,z,t) = w_b(x,t) + w_s(x,t) + f_2(z)w_z(x,t) \end{cases} \tag{1}$$

This theory posits that the transverse displacement is categorized into three distinct components: the bending w_b, shear w_s and normal displacement w_z. Here, u represents the axial displacement along the x-axis. The shear shape function employed in this framework is derived from a third-order polynomial shear deformation beam theory, as established by [7], using Eqn. (2), where $f_2(z) = 1 - f_1'(z)$

$$f_1(z) = \frac{4h}{5}\sinh\left(\frac{5z}{4h}\right) + z\left(-cosh\left(\frac{5}{8}\right) + \frac{3}{20}cos\left(\frac{5}{8}\right)\right) \tag{2}$$

The formula for strain energy U, according to these theories, is as follows:

$$U = \frac{1}{2}\int_0^{l_e}\int_A \left(\sigma_{ij}\varepsilon_{ij}\right) dA dx \tag{3}$$

Hence σ_{ij} and ε_{ij} represents the stress tensor and the strain tensor respectively which are defined by the following equations:

$$\begin{cases} \varepsilon_{xx} = \dfrac{du}{dx} = \dfrac{du}{dx} - z\dfrac{d^2 w_b}{dx^2} - f_1 \dfrac{d^2 w_s}{dx^2} \\ \varepsilon_{zz} = \dfrac{dw}{dz} = \dfrac{df_2}{dz} w_z \\ \varepsilon_{xz} = \dfrac{1}{2}\left(\dfrac{du}{dz} + \dfrac{dw}{dx}\right) = \dfrac{1}{2} f_2 \left(\dfrac{dw_s}{dx} + \dfrac{dw_z}{dx}\right) \end{cases} \tag{4}$$

$$\begin{cases} \sigma_{xx} = (\lambda + 2\mu)\varepsilon_{xx} + \lambda\varepsilon_{zz} \\ \sigma_{xz} = 2\mu\gamma_{xz} \\ \sigma_{zz} = (\lambda + 2\mu)\varepsilon_{zz} + \lambda\varepsilon_{xx} \end{cases} \tag{5}$$

where

$$\mu = \frac{E}{2(1+\nu)} \tag{6}$$

$$\lambda = \frac{E\nu}{(1+\nu)(1-2\nu)} \tag{7}$$

Hence μ and λ are the Lame constants, and ν is the Poisson's ratio.
The substitution of Eqns. (4)-(7) in Eqn. (3) give:

$$\begin{aligned} U = \frac{1}{2}\int_0^{l_e} \Bigg[& I_1 \left(\frac{du}{dx}\right)^2 - 2_2 \frac{du}{dx}\frac{d^2 w_b}{dx^2} - 2I_3 \frac{du}{dx}\frac{d^2 w_s}{dx^2} + 2I_4 \frac{d^2 w_b}{dx^2}\frac{d^2 w_s}{dx^2} + I_5 \left(\frac{d^2 w_b}{dx^2}\right)^2 \\ & + I_6 \left(\frac{d^2 w_s}{dx^2}\right)^2 + I_7 w_z^2 + 2I_8 \frac{du}{dx} w_z - 2I_9 \frac{d^2 w_b}{dx^2} w_z - 2I_{10} \frac{d^2 w_s}{dx^2} w_z \\ & + I_{11} \left(\left(\frac{dw_s}{dx}\right)^2 + \left(\frac{dw_z}{dx}\right)^2 + 2\frac{dw_s}{dx}\frac{dw_z}{dx} \right) \Bigg] dx \end{aligned} \tag{8}$$

with:

$$\begin{aligned} \{I_{1:7}\} = (\lambda_s + 2\mu_s) & \left(b \int_{-\frac{b}{2}}^{\frac{b}{2}} \left(1, z, f_1, z f_1, z^2, f_1^2, \left(\frac{df_2}{dz}\right)^2\right) dz \right) + \left((\lambda_c - \lambda_s) + 2(\mu_c - \mu_s) \right) \\ & \left((b - 2e_s) \int_{\left(-\frac{b}{2} + e_s\right)}^{\left(\frac{b}{2} - e_s\right)} \left(1, z, f_1, z f_1, z^2, f_1^2, \left(\frac{df_2}{dz}\right)^2\right) dz \right) \end{aligned} \tag{9}$$

$$\{I_{8:10}\} = \lambda_s \left(b \int_{-\frac{b}{2}}^{\frac{b}{2}} \frac{df_2}{dz}(1, z, f_1) dz \right) + (\lambda_c - \lambda_s) \left((b - 2e_s) \int_{\left(-\frac{b}{2} + e_s\right)}^{\left(\frac{b}{2} - e_s\right)} \frac{df_2}{dz}(1, z, f_1) dz \right) \tag{10}$$

$$\{I_{11}\}=\mu_s\left(b\int_{-\frac{b}{2}}^{\frac{b}{2}}f_2{}^2dz\right)+\left(\mu_c-\mu_s\right)\left(\left(b-2e_s\right)\int_{\left(-\frac{b}{2}+e_s\right)}^{\left(\frac{b}{2}-e_s\right)}f_2{}^2dz\right) \tag{11}$$

The Kinetic Energy T can be written as:

$$\begin{aligned}T=\frac{1}{2}\int_0^{l_e}\Big[&J_1\left(\dot{u}^2+\dot{w}_b{}^2+\dot{w}_s{}^2+2\dot{w}_b\dot{w}_s\right)-2J_2\dot{u}\frac{d\dot{w}_b}{dx}+2J_3\dot{u}\frac{d\dot{w}_s}{dx}-2J_4\frac{d\dot{w}_b}{dx}\frac{d\dot{w}_s}{dx}+J_5\left(\frac{d\dot{w}_b}{dx}\right)^2+\\&+J_6\left(\frac{d\dot{w}_s}{dx}\right)^2+J_7\dot{w}_z{}^2+2J_8\left(\dot{w}_b\dot{w}_z+\dot{w}_s\dot{w}_z\right)\Big]dx\end{aligned} \tag{12}$$

Hence the mass moments of inertia:

$$\begin{aligned}\{J_{1:8}\}=\rho_s&\left(b\int_{-\frac{b}{2}}^{\frac{b}{2}}\left(1,z,f_1,zf_1,z^2,f_1{}^2,f_2{}^2,f_2\right)dz\right)+\\&+\left(\rho_c-\rho_s\right)\left(\left(b-2e_s\right)\int_{\left(-\frac{b}{2}+e_s\right)}^{\left(\frac{b}{2}-e_s\right)}\left(1,z,f_1,zf_1,z^2,f_1{}^2,f_2{}^2,f_2\right)dz\right)\end{aligned} \tag{13}$$

with ρ_s, and ρ_c indicate density for steel box layer and inner composite concrete respectively.
The potential energy associated with the beam under an externally applied axial load is expressed as follows:

$$V=-\frac{1}{2}\int_0^{l_e}N_{cr}\left[\left(\frac{dw_b}{dx}\right)^2+\left(\frac{dw_s}{dx}\right)^2+2\frac{dw_b}{dx}\frac{dw_s}{dx}\right]dx \tag{14}$$

Cracked element

In this study, the stiffness reduction of the beam is modeled as a cross-sectional reduction correlated with the progression of crack depth [21], as depicted in Fig. 2. Two distinct crack types are analyzed: a crack in the steel box layer and a crack in the composite polymer concrete core, these cracks are assumed to be independent. The crack depths for these components are denoted as "$0\le a_s\le\frac{h}{2}$" (steel box layer) and "$0\le a_c\le\left(\frac{h}{2}-e_s\right)$" (composite core), respectively. To account for these degradation mechanisms, the coefficients in Eqns. (9)-(13) are formulated as follows ("sc" index mean steel box crack and "cc" index mean composite polymer concrete core crack):

$$\begin{aligned}\{I_{1:7}\}_{sc}=\left(\lambda_s+2\mu_s\right)&\left(b\int_{-\frac{b}{2}}^{\left(\frac{b}{2}-a_s\right)}\left(1,z,f_1,zf_1,z^2,f_1{}^2,\left(\frac{df_2}{dz}\right)^2\right)dz\right.\\&\left.-\left(b-2e_s\right)\int_{-\frac{b}{2}+e_s}^{\frac{b}{2}-e_s}\left(1,z,f_1,zf_1,z^2,f_1{}^2,\left(\frac{df_2}{dz}\right)^2\right)dz\right)\end{aligned} \tag{15}$$

$$\{I_{8:10}\}_{sc} = \lambda_s \left(b \int_{-\frac{h}{2}}^{\left(\frac{h}{2}-a_s\right)} \frac{df_2}{dz}(1,z,f_1)dz - (b-2e_s) \int_{-\frac{h}{2}+e_s}^{\frac{h}{2}-e_s} \frac{df_2}{dz}(1,z,f_1)dz \right) \tag{16}$$

$$\{I_{11}\}_{sc} = \mu_s \left(b \int_{-\frac{h}{2}}^{\left(\frac{h}{2}-a_s\right)} {f_2}^2 dz - (b-2e_s) \int_{-\frac{h}{2}+e_s}^{\frac{h}{2}-e_s} {f_2}^2 dz \right) \tag{17}$$

$$\{I_{1:7}\}_{cc} = (\lambda_c + 2\mu_c)(b-2e_s) \int_{\left(-\frac{h}{2}+e_s\right)}^{\left(\frac{h}{2}-e_s-a_c\right)} \left(1, z, f_1, zf_1, z^2, {f_1}^2, \left(\frac{df_2}{dz}\right)^2\right) dz \tag{18}$$

$$\{I_{8:10}\}_{cc} = \lambda_c (b-2e_s) \int_{\left(-\frac{h}{2}+e_s\right)}^{\left(\frac{h}{2}-e_s-a_c\right)} \frac{df_2}{dz}(1,z,f_1)dz \tag{19}$$

$$\{I_{11}\}_{cc} = \mu_c (b-2e_s) \int_{\left(-\frac{h}{2}+e_s\right)}^{\left(\frac{h}{2}-e_s-a_c\right)} {f_2}^2 dz \tag{20}$$

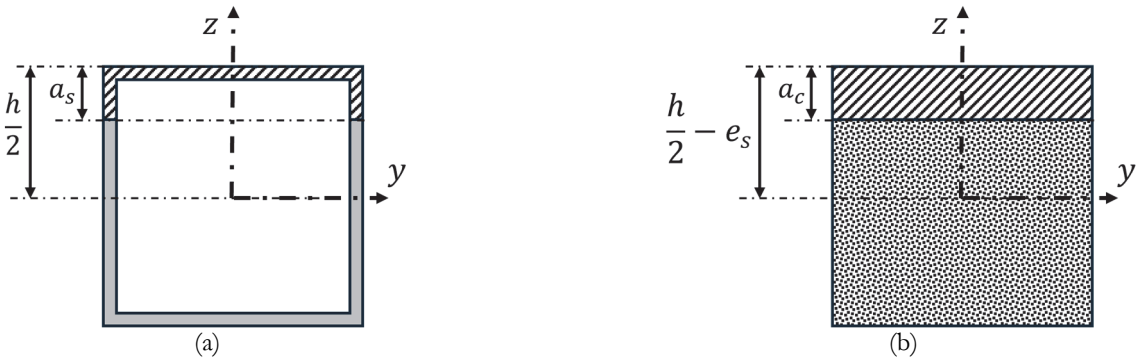

Figure 2: Cross section of the Cracked element. (a) (a_s crack depths of steel box layer), (b) (a_c crack depths composite polymer concrete core).

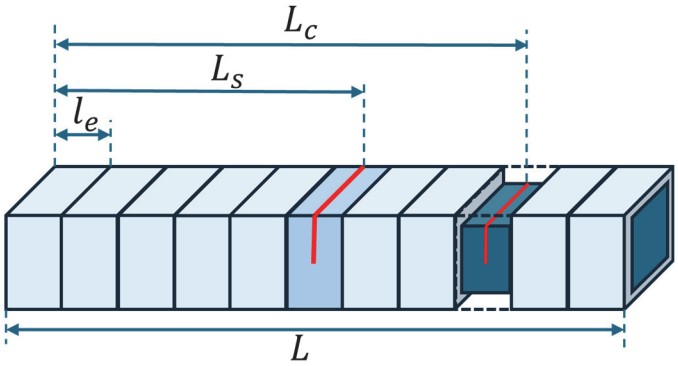

Figure 3: Crack position according to the mesh elements.

Since there are two types of cracks (Fig. 3), that of steel outer layer and that of inner composite polymer concrete. The crack location is indexed with L_s and L_c, where L_s and L_c represents the crack location from the left end of the beam for the steel outer layer and the inner composite polymer concrete respectively. l_e is the length of the mesh element.

DQFEM formulation

To represent our beam, we assume the shape functions take the form described in Eqn. (19) [9]:

$$\begin{aligned} u[x] &= \sum_{i=1}^{N} L_i(x)\bar{u}_i \ , \quad w_b[x] = \sum_{i=1}^{N} L_i(x)\bar{w}_b \\ w_s[x] &= \sum_{i=1}^{N} L_i(x)\bar{w}_s \ , \quad w_z[x] = \sum_{i=1}^{N} L_i(x)\bar{w}_z \end{aligned} \tag{21}$$

This formulation employs L_i to denote the Lagrange polynomial, while $\bar{u}_i = u(x_i)$, $\bar{w}_b = w_b(x_i)$, $\bar{w}_s = w_s(x_i)$ and $\bar{w}_z = w_z(x_i)$ represent the nodal displacements at the Gauss-Lobatto quadrature points within the differential quadrature (DQ) finite element framework of the beam. The nth-order derivative of a field variable f (x) at a discrete point x_i is approximated as follows:

$$\left.\frac{\partial^n f(x,t)}{\partial x^n}\right|_{x_i} = \sum_{j=1}^{N} A_{ij}^{(n)} f(x_j,t) \quad (i = 1,2,3,\ldots..,N) \tag{22}$$

In this context, $A_{ij}^{(n)}$ denotes the weighting coefficient associated with the nth order derivative approximation. $A_{ij}^{(n)}$ is derived as follows:

if n = 1, so

$$\begin{aligned} A_{ij}^{(1)} &= \frac{M(x_i)}{(x_i - x_j)M(x_j)} \quad i \neq j,\ i,j = 1,2,\ldots,N \\ A_{ii}^{(1)} &= -\sum_{j=1,\, j\neq i}^{n} A_{ij}^{(1)} \qquad i = 1,2,\ldots,N \end{aligned} \tag{23}$$

$$M(x_i) = \prod_{k=1,k\neq i}^{N} (x_i - x_k), \quad M(x_j) = \prod_{k=1,k\neq i}^{N} (x_j - x_k) \tag{24}$$

The Gauss-Lobatto quadrature rule, which possesses a degree of precision $2n-3$ for a function $f(x)$ defined within the interval $[-1,1]$, is expressed as follows:

$$\int_{-1}^{1} f(x)dx = \sum_{j=1}^{N} C_j f(x_j) \tag{25}$$

$$C_1 = C_N = \frac{2}{N(N-1)}, \quad C_j = \frac{2}{N(N-1)\left[P_{N-1}(x_j)\right]^2} \quad (j \neq 1,N) \tag{26}$$

x_j corresponds to the (j−1)-th root of the first derivative of the Legendre polynomial $P_{N-1}(x)$. To achieve fast convergence and high accuracy, a denser distribution of points near the boundaries is essential. Therefore, the sampling points are chosen based on the distribution of nodes in the Gauss–Lobatto grid and solved via Newton-Raphson iteration method.

$$x_j = -\cos\left(\frac{j-1}{N-1}\pi\right) \tag{27}$$

The relation between u and $\bar{u}$, w and $\bar{w}$ is defined using rule DQ [8]:

$$u = Q\bar{u}, \quad w_{b,s,z} = Q\bar{w}_{b,s,z} \tag{28}$$

where

$$Q = \begin{bmatrix} 1 & 0 & 0 & \cdots & 0 & 0 \\ A_{1,1}^{(1)} & A_{1,2}^{(1)} & A_{1,3}^{(1)} & \cdots & A_{1,N-1}^{(1)} & A_{1,N}^{(1)} \\ 0 & 0 & 1 & \cdots & 0 & 0 \\ \vdots & \vdots & \vdots & \ddots & \vdots & \vdots \\ 0 & 0 & 0 & \cdots & 0 & 1 \\ A_{N,1}^{(1)} & A_{N,2}^{(1)} & A_{N,3}^{(1)} & \cdots & A_{N,N-1}^{(1)} & A_{N,N}^{(1)} \end{bmatrix} \tag{29}$$

Utilizing the DQFEM, by substituting Eqns. (21-29) into Eqns. (8, 12, 14) and employing Lagrange's principle, we derive the subsequent elementaries matrixes.
The element mass matrix:

$$[M_e] = \begin{cases} [M_e]_{11} = \left[J_1 Q^T \bar{C} Q\right] \\ [M_e]_{12} = -\left[J_2 Q^T \bar{C} \bar{A}^{(1)} Q\right] \\ [M_e]_{13} = -\left[J_3 Q^T \bar{C} \bar{A}^{(1)} Q\right] \\ [M_e]_{22} = \left[J_1 Q^T \bar{C} G_b + J_5 Q^T \bar{A}^{(1)^T} \bar{C} \bar{A}^{(1)} Q\right] \\ [M_e]_{23} = \left[J_1 Q^T \bar{C} G_s + J_4 Q^T \bar{A}^{(1)^T} \bar{C} \bar{A}^{(1)} Q\right] \\ [M_e]_{24} = \left[J_8 Q^T \bar{C} Q\right] \\ [M_e]_{33} = \left[J_1 Q^T G_s + J_6 Q^T \bar{A}^{(1)^T} \bar{C} \bar{A}^{(1)} Q\right] \\ [M_e]_{34} = \left[J_8 Q^T \bar{C} Q\right] \\ [M_e]_{44} = \left[J_7 Q^T \bar{C} Q\right] \end{cases} \tag{30}$$

The element strain matrix:

$$
[K_e]=\begin{cases}
[K_e]_{11}=\left[I_1 Q^T \bar{A}^{(1)^T} \bar{C}\bar{A}^{(1)} Q\right] \\
[K_e]_{12}=-\left[I_2 Q^T \bar{A}^{(1)^T} \bar{C}\bar{A}^{(2)} Q\right] \\
[K_e]_{13}=-\left[I_3 Q^T \bar{A}^{(1)^T} \bar{C}\bar{A}^{(2)} Q\right] \\
[K_e]_{14}=\left[I_8 Q^T \bar{A}^{(1)^T} \bar{C} Q\right] \\
[K_e]_{22}=\left[I_5 Q^T \bar{A}^{(2)^T} \bar{C}\bar{A}^{(2)} Q\right]-N_{cr}\left[Q^T \bar{A}^{(1)^T} \bar{C}\bar{A}^{(1)} Q\right] \\
[K_e]_{23}=\left[I_4 Q^T \bar{A}^{(2)^T} \bar{C}\bar{A}^{(2)} Q\right]-N_{cr}\left[Q^T \bar{A}^{(1)^T} \bar{C}\bar{A}^{(1)} Q\right] \\
[K_e]_{24}=-\left[I_9 Q^T \bar{A}^{(2)^T} \bar{C} Q\right] \\
[K_e]_{33}=\left[I_6 Q^T \bar{A}^{(2)^T} \bar{C}\bar{A}^{(2)} Q+I_{11} Q^T \bar{A}^{(1)^T} \bar{C}\bar{A}^{(1)} Q\right]-N_{cr}\left[Q^T \bar{A}^{(1)^T} \bar{C}\bar{A}^{(1)} Q\right] \\
[K_e]_{34}=\left[I_{10} Q^T \bar{A}^{(2)^T} \bar{C} Q+I_{11} Q^T \bar{A}^{(1)^T} \bar{C}\bar{A}^{(1)} Q\right] \\
[K_e]_{44}=\left[I_7 Q^T \bar{C} Q+I_{11} Q^T \bar{A}^{(1)^T} \bar{C}\bar{A}^{(1)} Q\right]
\end{cases} \tag{31}
$$

The outer steel layer cracked element strain matrix:

$$
[K_{e_{SC}}]=\begin{cases}
[K_{e_{SC}}]_{11}=\left[I_{1_{SC}} Q^T \bar{A}^{(1)^T} \bar{C}\bar{A}^{(1)} Q\right] \\
[K_{e_{SC}}]_{12}=-\left[I_{2_{SC}} Q^T \bar{A}^{(1)^T} \bar{C}\bar{A}^{(2)} Q\right] \\
[K_{e_{SC}}]_{13}=-\left[I_{3_{SC}} Q^T \bar{A}^{(1)^T} \bar{C}\bar{A}^{(2)} Q\right] \\
[K_{e_{SC}}]_{14}=\left[I_{8_{SC}} Q^T \bar{A}^{(1)^T} \bar{C} Q\right] \\
[K_{e_{SC}}]_{22}=\left[I_{5_{SC}} Q^T \bar{A}^{(2)^T} \bar{C}\bar{A}^{(2)} Q\right] \\
[K_{e_{SC}}]_{23}=\left[I_{4_{SC}} Q^T \bar{A}^{(2)^T} \bar{C}\bar{A}^{(2)} Q\right] \\
[K_{e_{SC}}]_{24}=-\left[I_{9_{SC}} Q^T \bar{A}^{(2)^T} \bar{C} Q\right] \\
[K_{e_{SC}}]_{33}=\left[I_{6_{SC}} Q^T \bar{A}^{(2)^T} \bar{C}\bar{A}^{(2)} Q+I_{11_{SC}} Q^T \bar{A}^{(1)^T} \bar{C}\bar{A}^{(1)} Q\right] \\
[K_{e_{SC}}]_{34}=\left[I_{10_{SC}} Q^T \bar{A}^{(2)^T} \bar{C} Q+I_{11_{SC}} Q^T \bar{A}^{(1)^T} \bar{C}\bar{A}^{(1)} Q\right] \\
[K_{e_{SC}}]_{44}=\left[I_{7_{SC}} Q^T \bar{C} Q+I_{11_{SC}} Q^T \bar{A}^{(1)^T} \bar{C}\bar{A}^{(1)} Q\right]
\end{cases} \tag{32}
$$

The inner core cracked element strain matrix:

$$
\left[K_{e_{CC}}\right]=\begin{cases}
\left[K_{e_{CC}}\right]_{11}=\left[I_{1_{CC}}Q^{T}\overline{A}^{(1)^{T}}\overline{C}\overline{A}^{(1)}Q\right]\\
\left[K_{e_{CC}}\right]_{12}=-\left[I_{2_{CC}}Q^{T}\overline{A}^{(1)^{T}}\overline{C}\overline{A}^{(2)}Q\right]\\
\left[K_{e_{CC}}\right]_{13}=-\left[I_{3_{CC}}Q^{T}\overline{A}^{(1)^{T}}\overline{C}\overline{A}^{(2)}Q\right]\\
\left[K_{e_{CC}}\right]_{14}=\left[I_{8_{CC}}Q^{T}\overline{A}^{(1)^{T}}\overline{C}Q\right]\\
\left[K_{e_{CC}}\right]_{22}=\left[I_{5_{CC}}Q^{T}\overline{A}^{(2)^{T}}\overline{C}\overline{A}^{(2)}Q\right]\\
\left[K_{e_{CC}}\right]_{23}=\left[I_{4_{CC}}Q^{T}\overline{A}^{(2)^{T}}\overline{C}\overline{A}^{(2)}Q\right]\\
\left[K_{e_{CC}}\right]_{24}=-\left[I_{9_{CC}}Q^{T}\overline{A}^{(2)^{T}}\overline{C}Q\right]\\
\left[K_{e_{CC}}\right]_{33}=\left[I_{6_{CC}}Q^{T}\overline{A}^{(2)^{T}}\overline{C}\overline{A}^{(2)}Q+I_{11_{CC}}Q^{T}\overline{A}^{(1)^{T}}\overline{C}\overline{A}^{(1)}Q\right]\\
\left[K_{e_{CC}}\right]_{34}=\left[I_{10_{CC}}Q^{T}\overline{A}^{(2)^{T}}\overline{C}Q+I_{11_{CC}}Q^{T}\overline{A}^{(1)^{T}}\overline{C}\overline{A}^{(1)}Q\right]\\
\left[K_{e_{CC}}\right]_{44}=\left[I_{7_{CC}}Q^{T}\overline{C}Q+I_{11_{CC}}Q^{T}\overline{A}^{(1)^{T}}\overline{C}\overline{A}^{(1)}Q\right]
\end{cases}
\tag{33}
$$

The interval [-1, 1] is the only valid range for all kinds of node distributions in differentiation and quadrature. Therefore, the differential and quadrature matrices need to be adjusted as follows in order to put them into practice.

$$
\overline{C}=\frac{l_e}{2}C,\qquad \overline{A}^{(1)}=\frac{2}{l_e}A^{(1)},\qquad \overline{A}^{(2)}=\frac{4}{l_e^{\,2}}A^{(2)} \tag{34}
$$

l_e designate the beam element length.

The cracked element is introduced during the assembly step of the total strain matrix, so as to replace the strain matrix of the uncracked element with that of the cracked element. This substitution makes it possible to obtain the total strain matrix of the system as showed in Fig. 4.

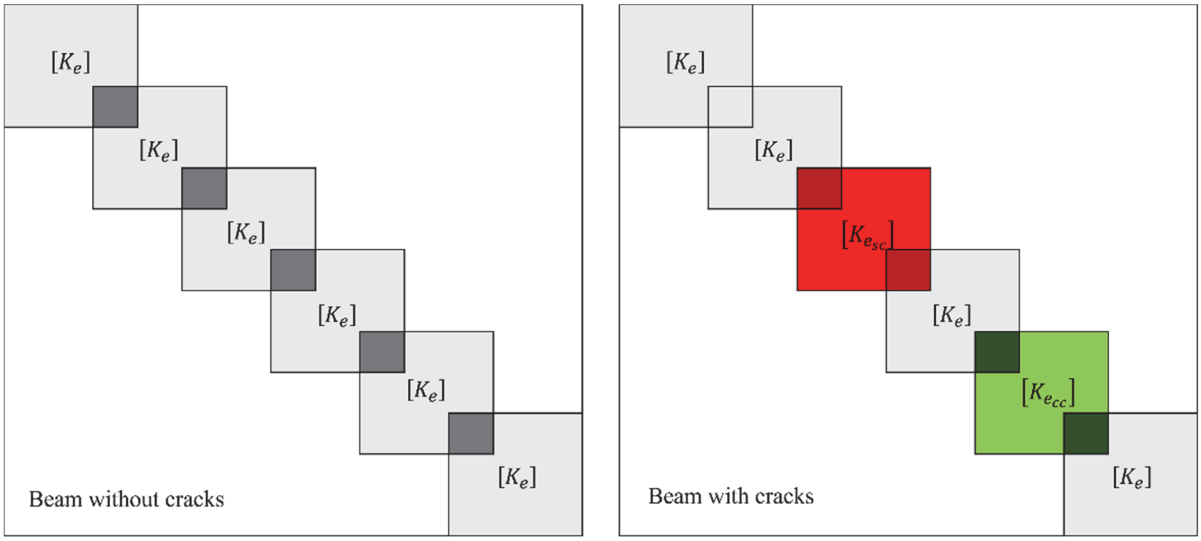

Figure 4: Global strain matrix with and without cracks

The global equation is as follow:

$$\left[[K]-\omega^2[\mathrm{M}]\right]\begin{Bmatrix} u \\ w_b \\ w_s \\ w_z \end{Bmatrix}=[0] \tag{35}$$

DISCUSSION OF RESULTS

A beam with box shape section inner composite material and metal as outer material shown in Fig. 1, is studied in this section. The material properties for the outer material (Steel): Young's modulus $E_{steel}=210\,GPa$, a mass density $\rho_{steel}=7812\,kg/m^3$, Poisson's ratio $\nu_{steel}=0.28$. The inner material used in this study is a composite polymer concrete [6] : Young's modulus $E_{concrete}=17.2\,GPa$, a mass density $\rho_{concrete}=2200\,kg/m^3$, Poisson's ratio $\nu_{concrete}=0.20$. In order to examine the current models, a comparative search is first carried out with the literature (Tab. 1), for a beam made from a steel profile measuring $L=1000\,mm$ in length, featuring a square cross-section with dimensions of thickness $h=70\,mm$, and a width $b=70\,mm$ and a wall thickness of $e_s=3\,mm$, which is internally filled with polymer concrete.

Model	Experimental [6]	FEM. TBT [6]	DQFEM. Q3D	DQFEM. TBT	DQFEM. EBT
1	339	338	340	337	352
2	899	915	905	880	962
3	1669	1755	1659	1618	1863
4	2572	2833	2595	2495	3027
5	3589	4124	3605	3471	3957

Table 1: Natural frequencies (Hz) comparison with literature.

Tab. 1 shows the natural frequencies of the composite beam predicted by the DQFEM-Q3D model closely match experimental results (≤1.5% deviation), validating its accuracy. In contrast, the frequencies obtained in this study for classical beam theories show limitations: Timoshenko beam theory (TBT) underestimates higher-mode frequencies (e.g., Mode 5: 3471 Hz vs. experimental 3589 Hz), while Euler Bernoulli beam theory (EBT) overestimates them significantly (e.g., Mode 5: 3957 Hz, 10.3% error). The literature's FEM model via TBT also overestimates higher modes (e.g., Mode 4: 2833 Hz vs. experimental 2572 Hz). These results confirm that the quasi-3D theory via DQFEM, which accounts for shear and material complexity, outperforms simplified models, making it ideal for dynamic analysis of composite beams.

The impact of the depth of the crack $\overline{a}_s=2a_s/h$, $\overline{a}_c=2a_c/\left(\frac{h}{2}-e_s\right)$ and location $\overline{l}_s=L_s/L$, $\overline{l}_c=L_c/L$ on the frequencies and the critical buckling is analyzed, where L_s and L_c represents the crack location from the left end of the beam for the steel outer layer and the inner composite polymer concrete respectively. To facilitate ease of use in the parametric study, the nondimensional parameters outlined below are employed for all results presented in Tables and Figures.

The frequency parameter ($\overline{\omega}$):

$$\overline{\omega}=\frac{\omega L^2}{h}\sqrt{\frac{\rho_s}{E_s}} \tag{36}$$

The Critical buckling load parameter ($\overline{N}_{cr}$):

$$\bar{N}_{cr} = \frac{12 N_{cr} L^2}{E_s b h^3} \tag{37}$$

In the following tables, the results are presented for different boundary conditions: Simply-Supported-Simply-Supported (S-S), Clamped-Clamped (C-C), and Clamped-Free (C-F). These boundary conditions represent distinct support configurations that significantly influence the dynamic behavior of the beam, including its natural frequencies and critical buckling loads.

Non-dimensional crack depth $\bar{a}_s$		Frequency parameter				
		0	0.25	0.5	0.75	1
S-S	$\bar{\omega}_1$	2.6711	2.6433	2.6350	2.6287	2.6251
	$\bar{\omega}_2$	10.3727	10.0768	9.9909	9.9281	9.8922
	$\bar{\omega}_3$	22.3181	21.5775	21.3750	21.2285	21.1440
C-C	$\bar{\omega}_1$	5.8866	5.8574	5.8494	5.8430	5.8386
	$\bar{\omega}_2$	15.6187	15.5544	15.5360	15.5214	15.5111
	$\bar{\omega}_3$	28.5679	28.0199	27.8555	27.7268	27.6430
C-F	$\bar{\omega}_1$	0.9582	0.9127	0.8995	0.8897	0.8838
	$\bar{\omega}_2$	5.8362	5.8118	5.8047	5.7989	5.7945
	$\bar{\omega}_3$	15.6695	15.5780	15.5440	15.5103	15.4799

Table 2: Effects of the steel outer layer crack depth $\bar{a}_s$, where $\bar{l}_s = 0.15$, on the frequency parameter. (uncracked inner core composite polymer concrete).

Non-dimensional crack depth $\bar{a}_s$		Critical buckling parameter				
		0	0.25	0.5	0.75	1
S-S	$\bar{N}_{cr1}$	3.5259	3.4488	3.4257	3.4084	3.3980
	$\bar{N}_{cr2}$	5.9663	4.7154	4.5529	4.3818	4.3449
	$\bar{N}_{cr3}$	5.9709	4.7344	4.5582	4.4020	4.3684
C-C	$\bar{N}_{cr1}$	5.9725	4.7158	4.5531	4.3818	4.3449
	$\bar{N}_{cr2}$	5.9726	4.7343	4.5581	4.4020	4.3684
	$\bar{N}_{cr3}$	5.9914	5.9572	5.9027	5.8018	5.7767
C-F	$\bar{N}_{cr1}$	0.8784	0.8134	0.7946	0.7805	0.7722
	$\bar{N}_{cr2}$	3.0722	3.0662	3.0646	3.0633	3.0626
	$\bar{N}_{cr3}$	5.9723	4.7151	4.5527	4.3816	4.3447

Table 3: Effects of the steel outer layer crack depth $\bar{a}_s$, where $\bar{l}_s = 0.15$, on the critical buckling parameter. (uncracked inner core composite polymer concrete).

Non-dimensional crack location $\overline{l}_s$		Frequency parameter				
		0.15	0.25	0.35	0.55	0.85
S-S	$\overline{\omega}_1$	2.6398	2.6058	2.5749	2.5568	2.6398
	$\overline{\omega}_2$	10.0401	9.9588	10.1158	10.3264	10.0401
	$\overline{\omega}_3$	21.4903	21.9814	22.2333	21.6440	21.4903
C-C	$\overline{\omega}_1$	5.8540	5.8731	5.7957	5.7233	5.8540
	$\overline{\omega}_2$	15.5466	15.1812	15.1895	15.5170	15.5466
	$\overline{\omega}_3$	27.9505	27.9649	28.4982	27.7916	27.9505
C-F	$\overline{\omega}_1$	0.9071	0.9219	0.9342	0.9506	0.9580
	$\overline{\omega}_2$	5.8088	5.8142	5.7110	5.5769	5.8063
	$\overline{\omega}_3$	15.5645	15.1540	15.2095	15.5278	15.3165

Table 4: Effects of the steel outer layer crack location $\overline{l}_s$, where $\overline{a}_s = 0.35$, on the frequency parameter. (uncracked inner core composite polymer concrete)

Non-dimensional crack location $\overline{l}_s$		Critical buckling parameter				
		0.15	0.25	0.35	0.55	0.85
S-S	$\overline{N}_{cr1}$	3.4389	3.3468	3.2662	3.2210	3.4389
	$\overline{N}_{cr2}$	4.6609	4.6615	4.6620	4.6623	4.6609
	$\overline{N}_{cr3}$	4.6686	4.6685	4.6685	4.6684	4.6686
C-C	$\overline{N}_{cr1}$	4.6612	4.6610	4.6608	4.6606	4.6612
	$\overline{N}_{cr2}$	4.6684	4.6684	4.6685	4.6685	4.6684
	$\overline{N}_{cr3}$	5.9447	5.9370	5.9354	5.9351	5.9447
C-F	$\overline{N}_{cr1}$	0.8054	0.8122	0.8212	0.8431	0.8724
	$\overline{N}_{cr2}$	3.0655	3.0678	3.0700	3.0721	3.0665
	$\overline{N}_{cr3}$	4.6607	4.6608	4.6607	4.6600	4.6598

Table 5: Effects of the steel outer layer crack location $\overline{l}_s$, where $\overline{a}_s = 0.35$, on the critical buckling parameter. (uncracked inner core composite polymer concrete).

Non-dimensional crack depth $\overline{a}_c$		Frequency parameter				
		0	0.25	0.5	0.75	1
S-S	$\overline{\omega}_1$	2.6711	2.6702	2.6695	2.6689	2.6684
	$\overline{\omega}_2$	10.3727	10.3630	10.3550	10.3487	10.3440
	$\overline{\omega}_3$	22.3181	22.2927	22.2720	22.2556	22.2435
C-C	$\overline{\omega}_1$	5.8866	5.8854	5.8844	5.8834	5.8826
	$\overline{\omega}_2$	15.6187	15.6162	15.6140	15.6121	15.6104
	$\overline{\omega}_3$	28.5679	28.5492	28.5334	28.5205	28.5104
C-F	$\overline{\omega}_1$	0.9582	0.9567	0.9555	0.9545	0.9538
	$\overline{\omega}_2$	5.8362	5.8352	5.8342	5.8334	5.8327
	$\overline{\omega}_3$	15.6695	15.6660	15.6627	15.6597	15.6568

Table 6: Effects of the inner core composite polymer concrete crack depth $\overline{a}_c$, where $\overline{l}_c = 0.15$, on the frequency parameter. (uncracked steel outer layer)

Non-dimensional crack depth $\bar{a}_c$		Critical buckling parameter				
		0	0.25	0.5	0.75	1
S-S	$\bar{N}_{cr1}$	3.5259	3.5236	3.5216	3.5200	3.5188
	$\bar{N}_{cr2}$	5.9663	5.9565	5.9265	5.8621	5.7654
	$\bar{N}_{cr3}$	5.9709	5.9676	5.9423	5.8840	5.8059
C-C	$\bar{N}_{cr1}$	5.9725	5.9681	5.9386	5.8673	5.7672
	$\bar{N}_{cr2}$	5.9726	5.9684	5.9437	5.8858	5.8069
	$\bar{N}_{cr3}$	5.9914	5.9841	5.9778	5.9764	5.9760
C-F	$\bar{N}_{cr1}$	0.8784	0.8763	0.8746	0.8732	0.8722
	$\bar{N}_{cr2}$	3.0722	3.0720	3.0718	3.0717	3.0716
	$\bar{N}_{cr3}$	5.9723	5.9681	5.9386	5.8673	5.7672

Table 7: Effects of the inner core composite polymer concrete crack depth $\bar{a}_c$, where $\bar{l}_c = 0.15$, on the critical buckling parameter. (uncracked steel outer layer).

Non-dimensional crack location $\bar{l}_c$		Frequency parameter				
		0.15	0.25	0.35	0.55	0.85
S-S	$\bar{\omega}_1$	2.6699	2.6686	2.6673	2.6666	2.6699
	$\bar{\omega}_2$	10.3596	10.3557	10.3619	10.3704	10.3596
	$\bar{\omega}_3$	22.2839	22.3025	22.3128	22.2896	22.2839
C-C	$\bar{\omega}_1$	5.8850	5.8859	5.8829	5.8800	5.8850
	$\bar{\omega}_2$	15.6153	15.6008	15.6001	15.6129	15.6153
	$\bar{\omega}_3$	28.5425	28.5415	28.5621	28.5346	28.5425
C-F	$\bar{\omega}_1$	0.9562	0.9568	0.9573	0.9579	0.9582
	$\bar{\omega}_2$	5.8348	5.8351	5.8312	5.8260	5.8350
	$\bar{\omega}_3$	15.6647	15.6509	15.6522	15.6632	15.6564

Table 8: Effects of the inner core composite polymer concrete crack location $\bar{l}_c$, where $\bar{a}_c = 0.35$, on the frequency parameter. (uncracked steel outer layer).

Non-dimensional crack location $\bar{l}_c$		Critical buckling parameter				
		0.15	0.25	0.35	0.55	0.85
S-S	$\bar{N}_{cr1}$	3.5227	3.5193	3.5160	3.5140	3.5227
	$\bar{N}_{cr2}$	5.9477	5.9501	5.9515	5.9525	5.9477
	$\bar{N}_{cr3}$	5.9620	5.9574	5.9552	5.9539	5.9620
C-C	$\bar{N}_{cr1}$	5.9613	5.9553	5.9534	5.9528	5.9613
	$\bar{N}_{cr2}$	5.9626	5.9574	5.9556	5.9549	5.9626
	$\bar{N}_{cr3}$	5.9806	5.9824	5.9860	5.9902	5.9806
C-F	$\bar{N}_{cr1}$	0.8756	0.8759	0.8762	0.8771	0.8782
	$\bar{N}_{cr2}$	3.0719	3.0720	3.0721	3.0722	3.0720
	$\bar{N}_{cr3}$	5.9613	5.9553	5.9534	5.9529	5.9599

Table 9: Effects of the inner core composite polymer concrete location $\bar{l}_c$, where $\bar{a}_c = 0.35$, on the critical buckling parameter (uncracked steel outer layer).

This study analyzes the dynamic and buckling behavior of quasi-3D steel-polymer concrete composite box beams with cracks, demonstrating that cracks in the steel outer layer drastically degrade performance: under simply supported (S-S) conditions, increasing the steel crack depth ($\bar{a}_s$) from 0 to 1 reduces the first natural frequency ($\bar{\omega}_1$) by 1.7% (2.6711 to 2.6251, Tab. 2) and the first critical buckling load ($\bar{N}_{cr1}$) by 3.6% (3.5259 to 3.3980, Tab. 3), while higher modes show greater sensitivity (e.g., simply supported (S-S) $\bar{\omega}_3$ drops 5.3% from 22.3181 to 21.1440, and $\bar{N}_{cr2}$ plummets 27.2% from 5.9663 to 4.3449); clamped-free (C-F) beams exhibit severe vulnerability, with $\bar{\omega}_1$ plunging 7.8% (0.9582 to 0.8838) and $\bar{N}_{cr1}$ collapsing 12.1% (0.8784 to 0.7722), whereas clamped-clamped (C-C) beams resist crack effects better (e.g., $\bar{\omega}_1$ drops only 0.8%, 5.8866 to 5.8386). Crack location in steel ($\bar{l}_s$) further modulates responses: mid-span cracks ($\bar{l}_s$ =0.55) minimize simply supported (S-S) $\bar{\omega}_1$ to 2.5568 (Tab. 4) and reduce $\bar{N}_{cr1}$ by 6.1% (3.4389 to 3.2210, Tab. 5), while cracks near supports ($\bar{l}_s$ =0.85) restore performance (e.g., simply supported (S-S) $\bar{\omega}_1$ rebounds to 2.6398), and clamped-free $\bar{N}_{cr1}$ rises 8.3% (0.8054 to 0.8724) as cracks shift toward the free end. In contrast, cracks in the polymer concrete core ($\bar{a}_c$, $\bar{l}_c$) have negligible impact: even at full depth ($\bar{a}_c$ =1), S-S $\bar{\omega}_1$ decreases by 0.1% (2.6711 to 2.6684, Tab. 6), and $\bar{N}_{cr2}$ drops 3.4% (5.9663 to 5.7654, Tab. 7), with crack location ($\bar{l}_c$) causing ≤0.2% frequency variation (e.g., simply supported (S-S) $\bar{\omega}_1$ ranges 2.6666–2.6699, Tab. 8) and ≤0.3% buckling fluctuation (e.g., S-S $\bar{N}_{cr1}$ varies 3.5140–3.5227, Tab. 9). Boundary conditions critically influence outcomes: C-C beams stabilize buckling loads (e.g., $\bar{N}_{cr3}$ declines only 3.2%, 28.5679 to 27.6430, Tab. 3) and suppress crack-location effects (e.g., $\bar{\omega}_3$ fluctuates <0.1%, 28.5346–28.5621, Tab. 8), while C-F beams suffer catastrophic steel-crack sensitivity (e.g., $\bar{\omega}_1$ drops 7.8% and $\bar{N}_{cr1}$ 12.1%) but ignore concrete cracks ($\bar{N}_{cr1}$ decreases 0.7%, 0.8784 to 0.8722, Tab. 7). The results confirm steel's dominance in structural integrity (steel's modulus $E_{steel} / E_{concrete} \approx 12.2$), with mid-span steel cracks most critical due to peak bending moments, while polymer concrete cracks are trivial, advocating prioritized steel-layer maintenance and validating the DQFEM model for crack-effect analysis in composite beams. Results in Tabs. (2-9) are illustrated in Figs. (5-6) for better visualization of the effect of the crack presence on the frequencies and critical buckling.

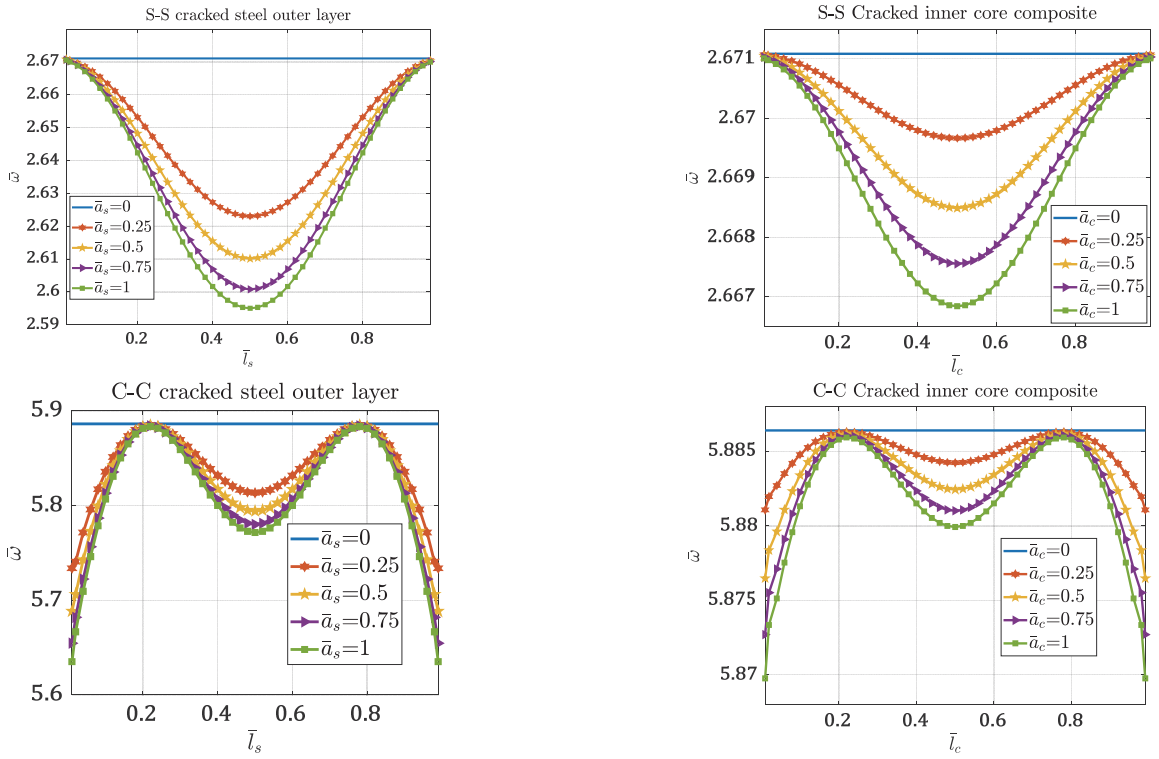

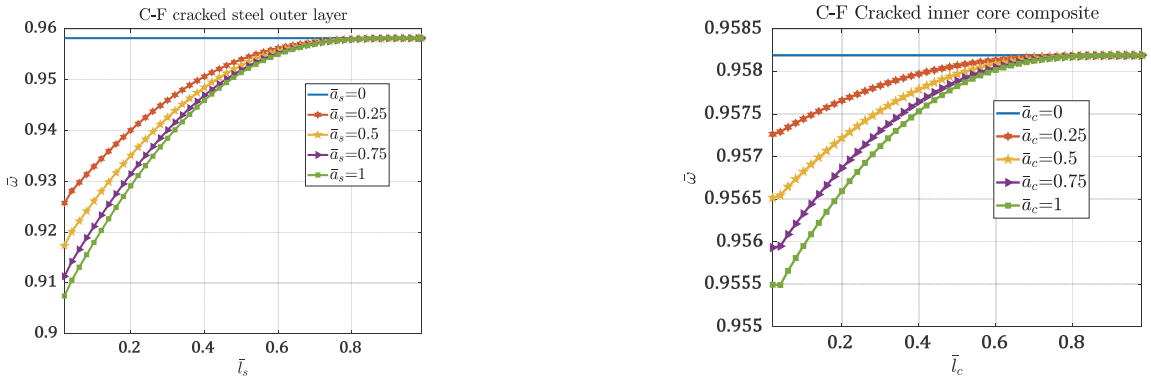

Figure 5: Crack location effect on the frequency's parameters of the beam for different boundary conditions and crack depth.

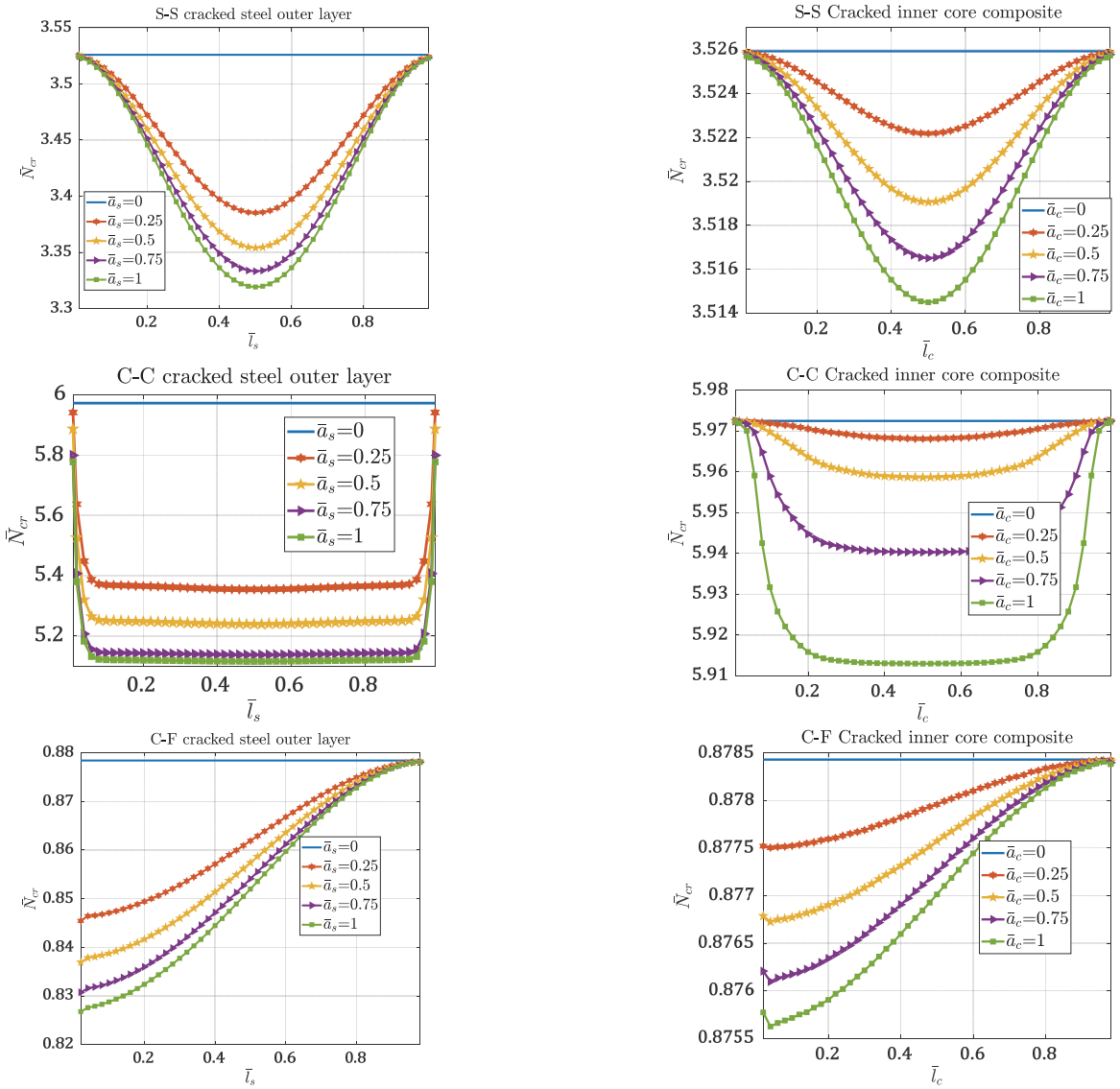

Figure 6: Crack location effect on the critical buckling parameter of the beam for different boundary conditions and crack depth.

Figs. 5 and 6 illustrate the influence of crack location (steel outer layer vs. inner composite polymer concrete core) on frequencies and critical buckling parameters of the box beam under varying boundary conditions (simply supported (S-S), clamped-clamped (C-C), clamped-free (C-F)) and crack depths. For S-S beams, the critical crack location is consistently at the midspan for both frequencies and buckling, regardless of crack depth or material (steel/composite), with symmetric

responses across crack positions. In C-C beams, frequencies exhibit dual critical regions: reductions occur near the supports and midspan, while values at the quarter-span closely match those of the uncracked beam; conversely, critical buckling parameters approach uncracked-beam levels when cracks are near the boundaries but remain nearly constant between midspan and quarter-span, indicating positional insensitivity in this zone. For C-F beams, frequencies are minimized at the clamped end but recover to near-uncracked values at the free end, with asymmetric responses and heightened sensitivity to crack position compared to S-S and C-C cases. Crack depth effects (Figs. 7–8) show a universal decline in frequencies with increasing depth across all boundaries and materials. For buckling, C-C beams with steel cracks exhibit clustered values across depths, suggesting limited depth dependency, while composite core cracks in C-C beams display nonlinear behavior: buckling remains stable up to a depth ratio of 0.5 before sharply declining, with spatial variations (e.g., midspan cracks induce the most severe degradation). Symmetry governs S-S and C-C responses, while asymmetry defines C-F behavior, with midspan cracks dominating S-S failures, C-C vulnerabilities concentrated near boundaries/midspan, and material-dependent buckling collapse (composite cores degrade abruptly beyond critical depths). These trends underscore the interplay of boundary constraints, crack geometry (location/depth), and material composition in determining structural stability.

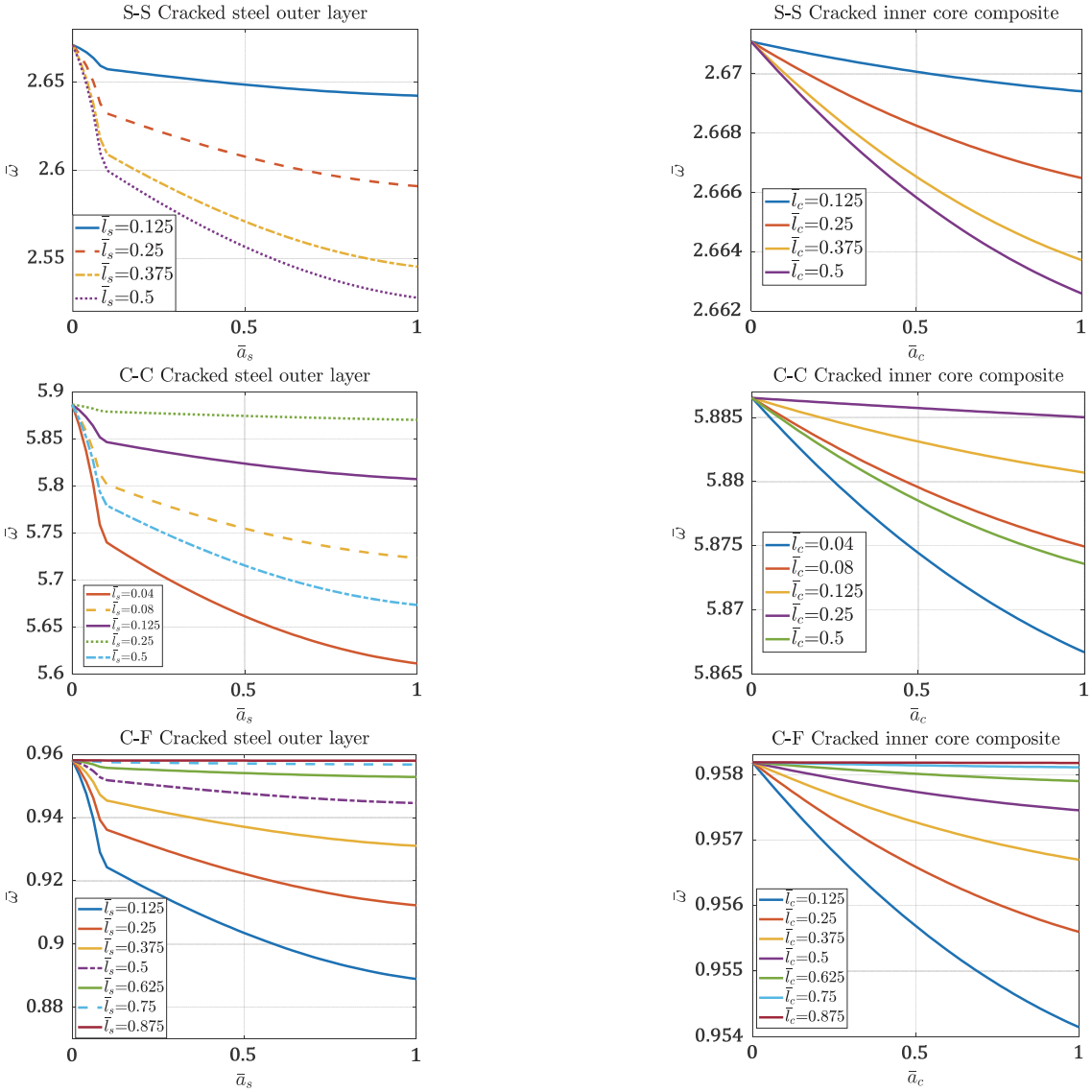

Figure 7: Crack depth effect on the frequency's parameters of the beam for different boundary conditions and crack location

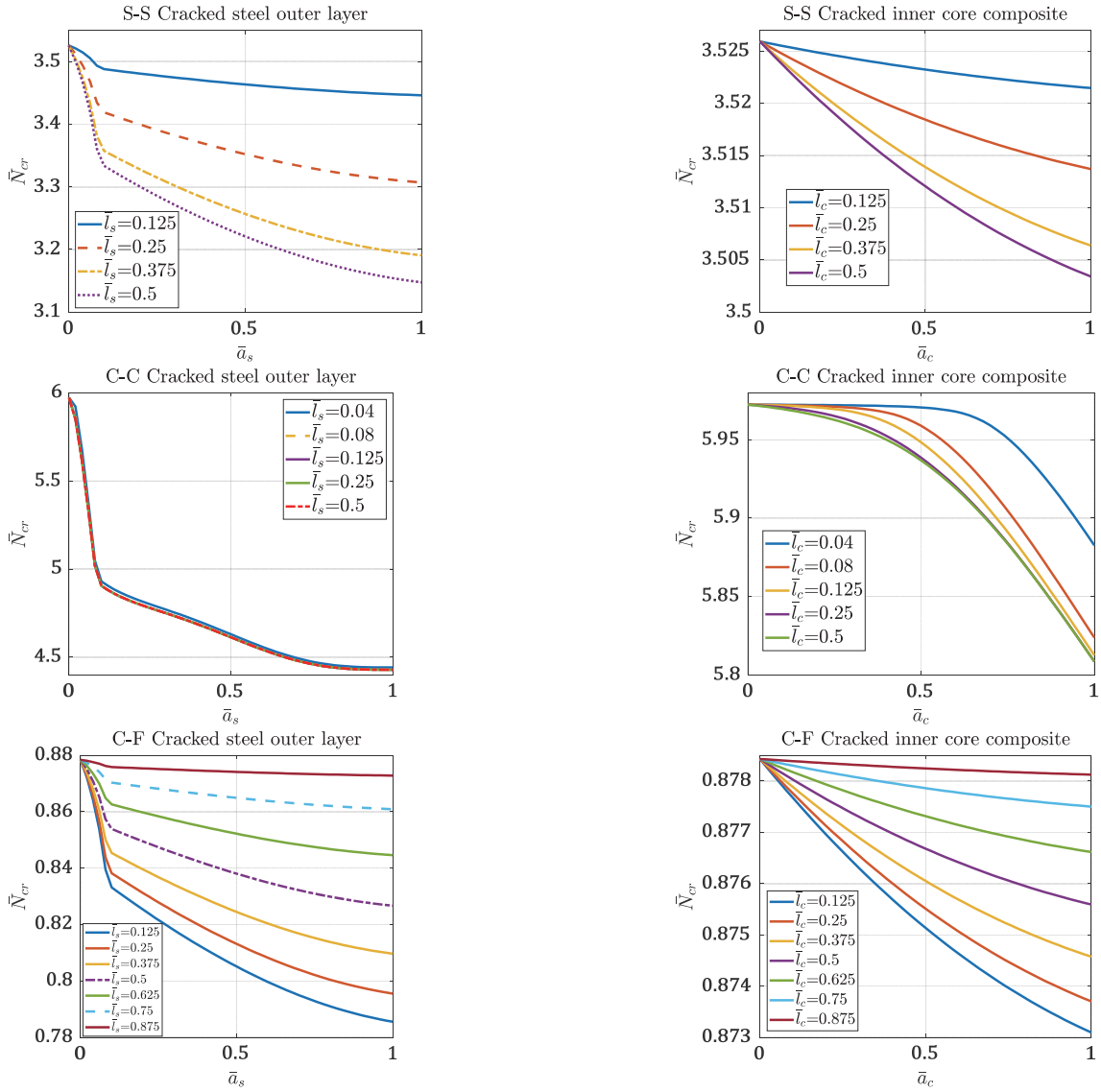

Figure 8: Crack depth effect on the critical buckling parameter of the beam for different boundary conditions and crack location

CONCLUSION

This study employed the Differential Quadrature Finite Element Method (DQFEM) integrated with quasi-3D beam theory to investigate the dynamic and buckling behavior of steel-polymer concrete composite box beams with cracks. The analysis focused on cracks in both the steel outer layer and the polymer concrete core, evaluating their effects under varying boundary conditions (simply supported [S-S], clamped-clamped [C-C], clamped-free [C-F]), crack depths, and locations. Key findings demonstrate that steel-layer cracks induce severe degradation: in C-F beams. Conversely, polymer concrete core cracks exhibited negligible impact, with frequency reductions ≤0.1% even at full depth. Crack location critically modulated responses: midspan cracks dominated S-S beam failures (symmetric frequency/buckling reductions), while C-C beams showed dual vulnerabilities near boundaries and midspan, with positional insensitivity in buckling between midspan and quarter-span. Boundary conditions profoundly influenced outcomes: C-F beams displayed asymmetric behavior, with catastrophic sensitivity to steel cracks near the clamped end, while C-C beams resisted buckling degradation until critical composite crack depths ($\bar{a}_c$ >0.5), beyond which nonlinear collapse occurred. The DQFEM model demonstrated high accuracy, validated against experimental and numerical benchmarks (e.g., ≤1.5% deviation in natural frequencies, Tab. 1). Parametric studies using non-dimensional crack parameters underscored steel's dominance in structural integrity (steel-to-concrete modulus ratio), with midspan steel cracks most critical due to peak

bending moments. These results emphasize the necessity of prioritizing steel-layer maintenance in composite beam design, particularly for dynamic and stability-critical applications. The study advances predictive frameworks for crack-induced degradation in quasi-3D systems, offering engineers actionable insights to enhance the resilience of material-based structures under complex loading scenarios.

This study advances predictive frameworks for crack-induced degradation in composite beams, offering engineers actionable insights to: Optimize material distribution (e.g., steel reinforcement at midspan for S-S beams). Enhance inspection protocols for high-risk zones (e.g., clamped ends in C-F beams). Improve resilience in dynamic or stability-critical applications (e.g., aerospace, civil infrastructure). By bridging theoretical modeling (quasi-3D DQFEM) with practical design strategies, this work underscores the critical interplay of boundary constraints, crack geometry, and material heterogeneity in governing structural stability, paving the way for next-generation composite beam systems.

DISCLOSURE STATEMENT

No potential conflict of interest was reported by the author(s).

DATA AVAILABILITY STATEMENT

The authors declare that the data are available within the article.

FUNDING AND/OR CONFLICTS OF INTERESTS

No potential conflict of interest was reported by the author(s).

REFERENCES

[1] Han, S.-C., Kreja, I., Rus, G. and Lomboy, G. R. (2016). Structural Dynamics and Stability of Composite Structures, Advances in Materials Science and Engineering, 1, p. 7468181, DOI: 10.1155/2016/7468181.

[2] Dunaj, P., Berczyński, S., Chodźko, M. and Niesterowicz, B. (2020). Finite Element Modeling of the Dynamic Properties of Composite Steel–Polymer Concrete Beams, Materials, 13(7), p. 1630]. https://www.mdpi.com/1996-1944/13/7/1630.

[3] Zou, G. P., Xia, P. X., Shen, X. H. and Wang, P. (2017). Mechanical properties analysis of steel– concrete–steel composite beam, Journal of Sandwich Structures & Materials, 19(5), pp. 525-543, DOI: 10.1177/1099636215622949.

[4] Dahmane, M., Benadouda, M., Bennai, R., Saimi, A. and Atmane, H. A. (2024). Effect of crack on the dynamic response of bidirectional porous functionally graded beams on an elastic foundation based on finite element method, Acta Mechanica, 235(6), pp. 3849-3860. DOI: 10.1007/s00707-024-03906-1.

[5] Berczyński, S. and Wróblewski, T. (2005). Vibration of Steel–Concrete Composite Beams Using the Timoshenko Beam Model, Journal of Vibration and Control, 11(6), pp. 829-848. DOI: 10.1177/1077546305054678.

[6] Niesterowicz, B., Dunaj, P. and Berczyński, S. (2020). Timoshenko beam model for vibration analysis of composite steel-polymer concrete box beams, Journal of Theoretical and Applied Mechanics, 58(3), pp. 799-810. DOI: 10.15632/jtam-pl/122389.

[7] Mantari J. L. andGuedes Soares, C. (2014). Four-unknown quasi-3D shear deformation theory for advanced composite plates, Composite Structures, 109, pp. 231-239. DOI: 10.1016/j.compstruct.2013.10.047.

[8] Ahmed, S., Abdelhamid, H., Ismail, B. and Ahmed, F. (2021). An Differential Quadrature Finite Element and the Differential Quadrature Hierarchical Finite Element Methods for the Dynamics Analysis of on Board Shaft, European Journal of Computational Mechanics, 29(4-6), pp. 303–344, DOI: 10.13052/ejcm1779-7179.29461.

[9] Xing, Y. and Liu, B. (2009). High-accuracy differential quadrature finite element method and its application to free vibrations of thin plate with curvilinear domain, International Journal for Numerical Methods in Engineering, 80(13), pp. 1718-1742. DOI: 10.1002/nme.2685.

[10] Safaei, B. (2021). Frequency-dependent damped vibrations of multifunctional foam plates sandwiched and integrated by composite faces, The European Physical Journal Plus, 136(6), p. 646. DOI: 10.1140/epjp/s13360-021-01632-4.

[11] Yang, Z., Lu, H., Sahmani, S. and Safaei, B. (2021). Isogeometric couple stress continuum-based linear and nonlinear flexural responses of functionally graded composite microplates with variable thickness, Archives of Civil and Mechanical Engineering, 21(3), p. 114. DOI: 10.1007/s43452-021-00264-w.

[12] Liu, H.,Saeid, S. and Safaei, B. (2023). Nonlinear buckling mode transition analysis in nonlocal couple stress-based stability of FG piezoelectric nanoshells under thermo-electromechanical load, Mechanics of Advanced Materials and Structures, 30(16), pp. 3385-3405. DOI: 10.1080/15376494.2022.2073620.

[13] Milić, P., Marinković, D., Klinge, S. and Ćojbašić, Ž. (2023). Reissner-Mindlin based isogeometric finite element formulation for piezoelectric active laminated shells, Tehnički vjesnik, 30(2), pp. 416-425.

[14] Alshenawy, R., Safaei, B., Sahmani, S., Elmoghazy, Y., Al-Alwan, A. and Nuwairan, M. A. (2022). Buckling mode transition in nonlinear strain gradient-based stability behavior of axial-thermal-electrical loaded FG piezoelectric cylindrical panels at microscale, Engineering Analysis with Boundary Elements, 141, pp. 36-64. DOI: 10.1016/j.enganabound.2022.04.010.

[15] Sahmani, S., Rabczuk, T., Song, J.-H. and Safaei, B. (2025). Unified nonlocal surface elastic-based thermal induced asymmetric nonlinear buckling of inhomogeneous nano-arches subjected to dissimilar end conditions, Composite Structures, 357, p. 118961. DOI: 10.1016/j.compstruct.2025.118961.

[16] Feng, J., Gao, C., Safaei, B., Qin, Z., Wu, H., Chu, F., Scarpa, F. (2025). Exceptional damping of CFRPs: Unveiling the impact of carbon fiber surface treatments, Composites Part B: Engineering, 290, p. 111973. DOI: 10.1016/j.compositesb.2024.111973.

[17] Saimi, A., Bensaid, I. and Fellah, A. (2023). Effect of crack presence on the dynamic and buckling responses of bidirectional functionally graded beams based on quasi-3D beam model and differential quadrature finite element method, Archive of Applied Mechanics. DOI: 10.1007/s00419-023-02429-w.

[18] Saimi, A., Bensaid, I. and Civalek, Ö. (2023). A study on the crack presence effect on dynamical behaviour of bi-directional compositionally imperfect material graded micro beams, Composite Structures, 316, p. 117032. DOI: 10.1016/j.compstruct.2023.117032.

[19] Khiem, N. T., Hai, T. T. and Huong, L. Q. (2023). Modal analysis of cracked FGM beam with piezoelectric layer, Mechanics Based Design of Structures and Machines, 51(9), pp. 5120-5140. DOI: 10.1080/15397734.2021.1992775.

[20] Khiem, N. T., Tran, H. T. and Nam, D. (2020). Modal analysis of cracked continuous Timoshenko beam made of functionally graded material, Mechanics Based Design of Structures and Machines, 48(4), pp. 459-479. DOI: 10.1080/15397734.2019.1639518.

[21] Hassaine, N., Touat, N., Dahak, M., Fellah, A. and Saimi, A. (2024). Study of crack's effect on the natural frequencies of bi-directional functionally graded beam, Mechanics Based Design of Structures and Machines, 52(1), pp. 375-385. DOI: 10.1080/15397734.2022.2113408.

[22] Rizov, V. (2017). Analysis of longitudinal cracked two-dimensional functionally graded beams exhibiting material non-linearity, Fracture and Structural Integrity, 11(41), pp. 491-503. DOI: 10.3221/IGF-ESIS.41.61.

[23] Benaoum, F., Khelil, F. and Benhamena, A. (2020, Numerical analysis of reinforced concrete beams pre cracked reinforced by composite materials, Fracture and Structural Integrity, 14(54), pp. 282-296. DOI: 10.3221/IGF-ESIS.54.20.

[24] Namdar, A., Darvishi, E., Feng, X., Zakaria, I. and Yahaya, F. M. (2016). Effect of flexural crack on plain concrete beam failure mechanism A numerical simulation, Fracture and Structural Integrity, 10(36), pp. 168-181. DOI: 10.3221/IGF-ESIS.36.17.